EUROPEAN ORGANIZATION FOR NUCLEAR RESEARCH

CERN-EP/81-40
4 May 1981

THE (3π)-NUCLEON COLLISION IN COHERENT PRODUCTION ON NUCLEI AT 40 GeV/c

G. Bellini[1*], L.P. Chernenko[2], V.S. Datsko[2], M. di Corato[1*], P.L. Frabetti[3*], Yu.I. Ivanshin[2], P. Laurikainen[4], L.K. Litkin[2], P.F. Manfredi[5*], S. Micheletti[1*], V.A. Moiseenko[2], V.I. Nikanorov[2], S. Otwinowski[6], F. Palombo[1*], J. Pernegr[1*], M. Pernicka[7*], M. Pimiä[4*], A.F. Pisarev[2], I.L. Pisarev[2], A. Sala[1*], S. Sala[1*], S.I. Sychkov[2], M. Szeptycka[6], A.A. Tjapkin[2], I.M. Vassilevski[2], G. Vegni[1*], V.V. Vishniakov[2], O.A. Zaimidoroga[2], V.V. Antipov[2], A.G. Galperin[2], L. Moroni[1*] and V.A. Petrov[2]

(Submitted to Nuclear Physics)

* Visitor at CERN, Geneva, Switzerland.
1 Istituto di Fisica dell'Università and INFN, Milan, Italy.
2 Joint Institute for Nuclear Research, Dubna, USSR.
3 Istituto di Fisica dell'Università and INFN, Bologna, Italy.
4 High-Energy Physics Department, University of Helsinki, Finland.
5 Politecnico and INFN, Milan, Italy. Now at Facoltà di Ingegneria, Università di Pavia, Italy.
6 Institute of Nuclear Research, Warsaw, Poland.
7 Institut für Hochenergiephysik, Österreichische Akademie der Wissenschaften, Vienna, Austria.

ABSTRACT

The coherent 3π production on nine different nuclear targets has been studied using a 40 GeV/c π^- beam at the Serpukhov accelerator (CERN-Serpukhov experiment No. 5).

The absorption in nuclear matter of the produced system has been measured, analysing the data on the different nuclear targets. Identical results are obtained from the differential cross-sections and from the coherent nuclear cross-sections. The 1^+ waves show a very weak absorption, definitely smaller than 0^- and 2^- waves. No influence on the absorption comes from the spin-flip amplitudes, which have been found to be negligible in the coherent region.

The partial-wave contributions change not only with the nuclear target, but also with t'. The interpretation of these results, taking into account also our finding of the t' and A dependence of the relative phases, is now under investigation (overlapping resonances, interferences between resonances and non-resonant contribution, intermediate or transition states in the hadron-hadron collision processes?).

1. INTRODUCTION

When used as a target in very high energy physics, the nucleus has to be considered as a large and highly dense volume of nuclear matter, where several scatterers are close to each other. This provides a good opportunity to study the processes inside a nucleus during a very short time, namely of the order of the average distance between adjacent nucleons, i.e. 2 fm $\simeq 10^{-23}$ s. So the new-born hadronic system, produced inside it, can interact with the nucleons before it reaches asymptotic conditions, making it possible to study the hadronic physics over very short distances.

Two classes of processes have been studied using the nucleus as target: the coherent production of exclusive channels, and the incoherent multiparticle production. The most striking result obtained from the experimental data is a new important property of the strong interactions: that the hadronic matter is transparent to fast secondaries.

The coherent production data have been analysed, until now, in the frame of the Kölbig-Margolis-Glauber model [1], where the weak absorption in nuclear matter gives small values of the parameter σ_2 [2-8].

Moreover the Glauber model simplifies the interaction mechanism too much, because it assumes that the production process is instantaneous and point-like. Otherwise a part of the data on the nucleus could be explained assuming that the excited matter, after the collision, passes through an intermediate step before a fixed state would be achieved. Many authors use different approaches to describe the behaviour of the "new-born" system [9-14], including a sequence of single productions in a multistep process [15].

In the description of the production process inside the nucleus the behaviour of the different spin-parity states as a function of the produced mass and of the four-momentum transfer is certainly very important. In addition, the study of the propagation of different partial amplitudes in nuclear matter can cast some new light on the mechanism of the hadron-hadron collision.

An experiment has been carried out at the Serpukhov accelerator by our collaboration (CERN-Serpukhov experiment No. 5) to study the coherent production on

nuclei at 40 GeV/c. A sample of ∿120,000 interactions of the channel

$$\pi^- A \to \pi^-\pi^-\pi^+ A \qquad (1)$$

was obtained from ∿500,000 triggers. Eight conventional nuclear targets (Be, C, Al, Ti, Cu, Ag, Ta, Pb) were used in addition to a live target consisting of 10 silicon detectors.

The data were fitted with the Kölbig-Margolis-Glauber model, in order to compare the results of this experiment with the behaviour at 15 GeV/c (refs. [2-4]) and 22 GeV/c (refs. [5-8]), and to represent with simple parameters the absorption in nuclear matter. Then fits on the total coherent cross-sections and on the differential cross-sections were done with different cuts on $t' = |t-t_{min}|$. The behaviour of the spin-parity states in the different nuclear targets and the possible contribution of spin-flip [16] are investigated.

In Sections 2 and 3 the experimental set-up is described, and the acceptance, resolution, and efficiency of the apparatus and the reconstruction chain are analysed. Sections 4 and 5 present the differential cross-sections and the total coherent cross-sections, and the results of the fits with the Kölbig-Margolis-Glauber model are discussed in detail. In Section 6 the partial-wave contributions in the samples of the events obtained on the different nuclear targets and for different 3π mass and t' are given. A final discussion on what we have learned from this analysis is included in Section 7.

2. EXPERIMENTAL SET-UP

The experiment has been carried out at the negative beam (B4) of the Serpukhov PS accelerator, with an energy around 40 GeV and a top intensity of $\sim 10^6$ particles/s. The range of the spilling time was 0.8-1.2 s; the momentum definition of the beam $\Delta p/p \sim 2\%$. The experimental set-up consists of five parts.

2.1 Transport system and beam monitoring telescope

The transport system downstream from the vertical and the horizontal collimators (fig. 1a) includes two bending magnets, which define the beam energy, and a quadrupole pair, which focalizes the beam on the target plane.

A set of scintillation counters gives the monitoring of the intensity and defines the trajectory of the beam. It consists of six counters in coincidence and three in anticoincidence (see figs. 1b and 1c), the last of which (F_2) is a cut cone placed 10 cm before the target. The beam profile in the target plane has 0.8 cm FWHM in the vertical direction and 1.2 cm in the horizontal one.

The direction of the incident particle is given by a spectrometer in the beam line (fig. 1a), consisting of 10 wire spark chambers (each including two wire planes, vertical and horizontal) 1 mm apart, and six double planes of multiwire proportional chambers (MWPCs), 1 or 2 mm apart. The last two MWPCs are placed as near as possible to the target, where the beam particle trajectory is slightly deflected by the fringing field of the forward magnet.

The average efficiency in reconstructing momentum and coordinates of the incident particles ranges from 90% to 95%.

Three gas Čerenkov counters, placed in the beam line, select pions or kaons with a full efficiency for the π beam and $\sim$5% contamination for the K beam.

Finally, a beam killer ($10 \times 10 \times 2$ cm^3) is placed behind the spectrometer to veto the non-interacting beam particles.

2.2 A veto counter system

The forward acceptance cone for the charged prongs is fixed so as to have at least 80 cm of measurable track length, corresponding to eight spark chamber gaps crossed by the particle. Taking into account that the target is placed $\sim$70 cm before the first spark chamber plane, the full acceptance angle is 30° (see fig. 1b).

A veto counter system for both neutral and charged particles defines the acceptance cone, following the previous requirements. It consists of a cylindrical scintillation counter (F_1) and two lead/scintillator sandwiches (R_i and G_i) (fig. 1c).

The cylindrical counter F_1 (1 cm thick; 50 cm long) rejects events with fast charged secondaries emitted at a large angle, and/or slow protons escaping from the target ($p \geq 100$ MeV/c). The lead/scintillator counters (6 radiation lengths) R_i, which surround the target, reject with negligible inefficiency the events with π^0's produced at a large angle; G_i, a lead/scintillator sandwich of 8 radiation lengths, vetoes γ-rays and charged particles between 30° and 45°.

2.3 The magnetic spectrometer

The events accepted by the trigger are detected by a big magnetic spectrometer (MIS). The useful volume of the magnet is $1.3 \times 1.5 \times 5$ m^3; the magnetic field intensity ranges from 17 to 21 kG. Fifty units of optical spark chambers, each with a 2 cm gap, fill the magnet aperture.

The planes of the chamber, each with a surface 1.2×1.1 m^2, consist of Al foils, 0.2 mm thick, supported by copper plates. In order to minimize the multiple scattering, the region of the copper frames was excluded from the useful volume (see fig. 1).

The detection efficiency of the chambers is 98% for three-prong events; they operate with a high-voltage rise-time of $\sim$30 ns and are filled with henogal.

The picture are taken by two cameras with 16° stereoview angle.

2.4 The counter hodoscope and the MWPC selecting the charged multiplicity

The events produced inside the acceptance cone are selected according to their charged prong number. This selection is obtained using a plastic scintillator hodoscope (N) and a MWPC, the fast majority signals of which are used in the trigger.

The plastic hodoscope (N_i counters, see fig. 1b) is used to introduce in the trigger a "majority 1" requirement ($\Sigma N \geq 1$) in order to reject the elastic scatterings which mostly go through the central hole of the counters.

The MWPC consists of two sense wire planes, 60×60 cm^2, 2 mm apart. It is placed between the eighth and the ninth spark chamber unit, far enough away from the target ($\sim$120 cm) to allow a good spatial resolution for the produced particles. The thresholds of the MWPC are adjusted to fit a "majority 2" requirement; the efficiency is $\sim$96% with the two planes in coincidence. Details of the characteristics of the MWPC and the associated electronics can be found elsewhere [17].

2.5 γ detector

A large-surface γ detector is placed behind the magnet (fig. 1b) to veto the forward π^0's. It consists of a lead/scintillator sandwich (four slabs) which converts the photons (γ_i), and of a plastic scintillator (γ_1) placed in front of the sandwich, which recognizes the charge of the particle.

The trigger signature is

$$T \cdot \bar{K} \cdot \bar{F}_1 \cdot (\overline{\sum R_i}) \cdot (\overline{\sum G_i}) \cdot (\overline{\bar{Y}_1 \sum_{Yi}}) \cdot (\sum N_i \geq 1) \cdot (\text{MWPC} \geq 2) \ ,$$

where T is the beam telescope signal.

The information from counters, wire spark chambers, and MWPCs was collected on magnetic tape through a CAMAC system using an HP 2100 computer.

3. ACCEPTANCE, RESOLUTION, AND EFFICIENCY

The geometrical acceptance of the apparatus as a function of t' and $M_{3\pi}$ was estimated by a Monte Carlo program. It is almost independent of t' [at least up to 0.5 $(GeV/c)^2$] and decreases smoothly from 100% to 85% when $M_{3\pi}$ ranges from 0.9 to 1.8 GeV/c^2. The data have been corrected for the acceptance.

About 500,000 pictures, including all the triggers collected with incident pions, have been measured by an HPD flying-spot digitizer of the "Centro Nazionale Analisi Fotogrammi" (CNAF) of INFN. Beam tracks and empty-target pictures were also measured to calibrate the apparatus and to evaluate the empty-target background in the data, respectively.

The geometrical and kinematical reconstruction was done with a modified version of ROMEO, which includes a vertex fit routine and a kinematical reconstruction. The inefficiency of the reconstruction chain from HPD to KIN has been carefully calculated for three-prong events by scanning ∿30,000 pictures, randomly selected from the total statistics. The events of this sample that were lost by the reconstruction programs have been recovered by means of an interactive graphic system [18] for calculating the efficiency as a function of the track momentum and angles. The results show an efficiency of ∿92%, almost independent of t' and $M_{3\pi}$ values. The main source of the inefficiency is represented by the pattern recognition process.

From the analysis of $K^- \to \pi^-\pi^-\pi^+$ events that decayed before the spectrometer, a K^- mass distribution has been obtained with a mean value 497.5 MeV and a standard deviation of 6.5 MeV.

Monte Carlo calculations, giving results in agreement with the experimental effective mass errors for K^- decays, predict $\sigma(p_T \text{ recoil}) \sim 17$ MeV/c, and $\sigma_{M_{3\pi}} \simeq$ $\simeq$ 26 MeV at ∿1.1 GeV, ∿30 MeV at 1.5 GeV, and ∿34 MeV at 1.7 GeV.

4. DIFFERENTIAL CROSS-SECTION AND MASS SPECTRA

Figures 2, 3, and 4 show the differential cross-section for eight conventional nuclear targets and for three different intervals of the produced 3π mass: 1.0-1.2, 1.2-1.5, and 1.5-1.8 GeV. The measured cross-sections are represented by crosses, the vertical bars being the statistical errors and the horizontal ones corresponding to a constant interval in the (3π) production angle. The empty-target contribution has been subtracted in the plots.

Owing to the different type of target and to the different trigger used for the live target, the data concerning the silicon are not taken into account for the cross-sections.

Figure 5 shows the differential cross-sections for three different 3π masses for the Ta target: as expected, the decreasing of the forward peak with increasing mass is not important at 40 GeV.

In order to study the three-pion mass distributions for coherent events, a t' cut is applied to the data at $t' = t'^*$, which corresponds to the first dip of the t' distributions. As the incoherent background decreases with decreasing t', the events in the first diffractive maximum ($0 < t' < t'^*$) represent an enriched sample of "coherent events" with a very small percentage of incoherent interactions. The distributions of $M_{3\pi}$ thus obtained (fig. 6) show a large peak in the A_1 region and a clear bump in the A_3 region. The A_2 resonance, as expected, is strongly depressed by the selection rules of the coherent process.

5. TOTAL CROSS-SECTION OF THE (3π)-NUCLEON INTERACTION

The distributions of the coherent data can be compared with the Kölbig-Margolis equations [1], based on the Glauber model in the optical limit. Table 1 gives the Kölbig-Margolis formula. The nuclear form factor $\tilde{F}(t',M)$ depends on different parameters: σ_1 is the total cross-section of the incident pion on the nucleon; σ_2 is a parameter which reproduces the absorption in nuclear matter and, in the hypothesis of the model, should be the cross-section of the three-pion system on the nucleon; α_1 and α_2 are the ratios of the real to the imaginary part of the

forward elastic scattering amplitudes of the pion on the nucleon and of the three-pion system on the nucleon, respectively; a and c are the two parameters of the Fermi distribution of the nuclear density; M is the invariant mass of the produced system. The form factor $\tilde{F}(t',M)$ includes also the phase factor $\left\{\exp[i\chi_{Coul}(b)]\right\}$ accounting for the elastic scattering of the incoming and outgoing particle in the nuclear Coulomb field: its contribution is very small.

In the Kölbig-Margolis model the coherent cross-section is written in the following way:

$$\frac{d\sigma_c}{dt'} = \left(\frac{d\sigma_N}{dt'}\right)_{t'=0} A^2 |\tilde{F}(t',M)|^2 \ , \qquad (2)$$

where $(d\sigma_N/dt')_{t'=0} = C_0(M)$ is the cross-section for (3π) production on a single nucleon at $t' = 0$. A different formula has also been used, replacing $(d\sigma_N/dt')_{t'=0}$ with the following expression:

$$\frac{d\sigma_N}{dt'} = C_0(M)\ e^{-B(M)t'} \ . \qquad (3)$$

The incoherent contribution $d\sigma_I/dt'$ has been corrected with the factor $S(t',M,A)$ to account for the experimental bias introduced in the incoherent events by the veto counter F_1 surrounding the target.

The differential cross-sections $d\sigma/dt'$ versus t' versus A, and the total cross-sections σ_c versus A, have been fitted using the formulas of Table 1 with the following procedure:

i) The slope B(M) is obtained by fitting with an exponential function the compilation of the $(d\sigma/dt')$ distributions of all targets in the high-t' range, where only incoherent events contribute to the statistics; B is found to be $\approx 8.0\ (GeV/c)^{-2}$ in the different mass regions.

ii) The incoherent background has been subtracted from the differential cross-section distributions using an incoherent cross-section $d\sigma_I/dt'$ of the form shown in Table 1; I_0 has been obtained for each target and for each $M_{3\pi}$ interval from the high-t' region $d\sigma/dt'$ experimental distribution. The incoherent distributions are represented by the broken line in the different $d\sigma/dt'$ (see figs. 2, 3, 4, and 5).

iii) The differential cross-sections have been integrated in the different mass intervals

$$\frac{d\sigma_c}{dt'} = \int_{M_1}^{M_2} \frac{d\sigma_c}{dt'dM} \tag{4}$$

where the limits M_1 and M_2 are: 1.0-1.2, 1.2-1.5, 1.5-1.8 GeV, and they are fitted versus t' and versus A. Two separate fits have been made, up to $t' = t'^*$ and up to $t' = 0.5$ $(GeV/c)^2$.

The experimental resolution is folded into the theoretical curves.

iv) Similar fits are given on the integrated coherent cross-sections:

$$\sigma_c(A_1, M_1, M_2) = \int_{M_1}^{M_2} dM \int_0^{\overline{t'}} dt' \frac{d\sigma_c^2}{dMdt'} , \tag{5}$$

with $\overline{t'} = t^*$ and $\overline{t'} = 0.5$ $(GeV/c)^2$; (M_1-M_2) intervals are the same as in the fits (iii).

v) In the fits (iii) and (iv), σ_1 and α_1 are fixed parameters and are assumed to be the same as on free protons, as obtained from the experiments on hydrogen [19].

vi) Since σ_2 and α_2 strongly affect each other in the fit, α_2 is considered a fixed parameter and some typical values are used: -0.5, 0.0, +0.5. On the other hand, some fits have also been tried with α_2 as a free parameter.

vii) Finally the fits have been made with only two free parameters: σ_2 and C_0. As for α_2, the B value has been tested leaving it as a free parameter in some fits.

All the fits obtained with the different assumptions explained before are very successful.

The full lines drawn in figs. 2, 3, 4, 5, and 7 are the results of the fit on the differential cross-sections and on the total coherent cross-sections [see (iii) and (iv)], made using the following conditions: $\alpha_2 = 0.0$ fixed; $(d\sigma_N/dt')_{t'=0}$ replaced in eq. (2) by eq. (3); $B = 0.8$ $(GeV/c)^{-2}$ fixed; the fit on the differential cross-sections extended up to $t' = 0.5$ $(GeV/c)^2$; $\overline{t'} = 0.5$ in the fit on the total coherent cross-sections [see (5)]; σ_2 and C_0 are free parameters.

The agreement between theoretical formulas and experimental points is always quite good. In the differential cross-sections the theoretical distributions reproduce very well the first and the second dip and the experimental behaviour in the first and in the second diffractive maximum.

The different assumptions on α_2 and on the upper t' limit in the fit do not influence the fitted curves. These curves are also independent of the use, in formula (2), of $(d\sigma/dt')_{t'=0}$ or of the exponential (3).

The two last statements are supported by the σ_2 and C_0 best fit values, obtained under different conditions. They are shown in Tables 2, 3, 4, 5: the first two concern the fits on the differential cross-sections, and the last two the fits on the total coherent cross-sections. The different assumptions on $d\sigma_N/dt'$ and the upper t' limits in the fits are specified at the top of the tables, while the assumptions on α_2 and B are reported in the left-hand columns. The statistical errors correspond to changing the χ^2 of the fit by one: they include also the uncertainty for the inefficiency corrections. The systematic errors correspond to the maximum fluctuations of the σ_2 and C_0 values, which are obtained removing in turn, from the fitted experimental points, the cross-section corresponding to one nuclear target.

The fits are surprisingly stable, also when α_2 or B are taken as free parameters: their best fit values are very near to 0.0 and 8.0 $(GeV/c)^{-2}$, respectively. The different values of σ_2 and C_0 resulting from the fits obtained with different conditions are consistent, each to other, within the errors.

The parameter σ_2 is always definitely smaller than 20 mb in the full range of the 3π mass. Comparing this result with the one obtained at lower energies [2,5] it seems that $\sigma_2(3\pi)$ tends to decrease with increasing energy.

The parameter C_0 should be compared with the diffractive cross-section at $t' = 0$ for $\pi^-\pi^-\pi^+$ production on hydrogen. The total forward cross-sections on hydrogen can be deduced from the data of Antipov et al. [19] obtained at 40 GeV/c: 1.3 mb/GeV^2 for $1.0 < M_{3\pi} < 1.2$ GeV; 1.1 mb/GeV^2 for $1.2 < M_{3\pi} < 1.5$ GeV; and 0.75 mb/GeV^2 for $1.5 < M_{3\pi} < 1.8$ GeV. The C_0 obtained from our data shows the

typical values: $\sim$0.8 mb/GeV^2 for $1.0 < M_{3\pi} < 1.2$ GeV; $\sim$0.62 mb/GeV^2 for $1.2 < M_{3\pi} < 1.5$ GeV; and 0.35 mb/GeV^2 for $1.5 < M_{3\pi} < 1.8$ GeV.

6. PARTIAL WAVE ANALYSIS

The data have been analysed using the program PWA (Partial Wave Analysis) of the Illinois group [20]. The program has been adjusted for the nuclear targets and for the acceptance of our apparatus. The choice of the necessary waves has been made using the same criteria as those used by Pernegr et al. [21]. We keep the Illinois notation $J^P\ell M^\eta$ for the amplitudes; since amplitudes with $\eta = -1$ have not been found and states with $M \neq 0$ are needed rather rarely (except for the 2^+ states), we shall simply write $J^P\ell$ instead of $J^P\ell 0^+$.

To study the effective mass distributions of the partial waves, the events of all the targets have been put together and then divided into a "coherent" sample ($t' \leq t'^*$) and an "incoherent" sample of the remaining events.

The contributions of the important waves in the coherent sample are shown in fig. 8. The 2^+D1^+ wave (which is rather weak in the coherent sample) and the 1^+D amplitude (which is negligible in the low-mass region) are not included in the plot in order to not complicate the figure; in the A_3 region the 1^+D wave has about the same intensity as 1^+S or 1^+P waves.

The 1^+ state dominates everywhere in the coherent sample. It exhibits clear resonance properties in the A_1 region, but we cannot exclude that it consists of more than one resonance. The same is true about the 0^- state [22]. The 2^- waves confirm their resonance behaviour in the A_3 region [21,23].

To study the coherent production of partial amplitudes as a function of A and to maintain comparable statistics, the data from neighbouring elements have been grouped together as follows: Be + C, Al + Si, Ti + Cu, Ag + Ta + Pb. The weighted mean values of A are $\bar{A}$ = 10.5, 27.9, 56.0, 170.0, respectively.

In order to decrease the incoherent background, only events with $t' < 0.01$ (GeV/c)^2 have been taken into account. For the light nuclei this cut is more severe than the limitation on t' imposed in the previous analysis (see

Section 4), but it presents the advantage of defining coherent samples with an incoherent background, which is nearly the same for all the nuclear targets ($\simeq$ 6% for Be and 1.5% for Pb).

Since the t'-dependence of the different partial waves produced on a nucleus A is not necessarily identical and may change with A and $M_{3\pi}$, an arbitrary t' cut may influence the wave contributions in different samples. Therefore an analysis in small t' bins on all the groups of targets has been performed in the three mass regions: 0.9-1.2, 1.2-1.5, 1.5-1.8 GeV. As an example, fig. 9 shows the t' dependence of several amplitudes, produced on the lightest (Be + C) and on the heaviest (Ag + Ta + Pb) nuclei. The percentages are plotted in order to see small differences better than in the $d\sigma/dt'$ plots. We observe that whereas on light nuclei the contributions are rather constant (and the position of the t' cut is therefore not critical), on heavy nuclei they do change, mainly in the coherent region [$t' < 0.01$ (GeV/c)^2]. The presence of a small incoherent background ($\sim$2%) cannot have any influence on the observed changes.

The t'-dependence and A-dependence of the helicity-flip amplitudes (1^+1^+, 2^+1^+, 2^-1^+) have been studied in broader t' bins in order to reduce the errors. The results obtained for the lightest and the heaviest nuclear targets are presented in fig. 10. In the region of small t', the spin-flip amplitudes are almost negligible. In addition, correlations with higher waves (e.g. 1^+D in $M_{3\pi} < 1.2$ GeV region) tend to decrease their signals. Therefore we did not take them into account in any further analysis.

The contributions of all important partial waves are summarized in Table 6. Let us note that the percentage of a total J^P state is not simply the sum of the contributions of its partial waves, owing to the interference terms. We observe that the 0^- and 2^- contributions decrease systematically with increasing target mass, whilst 1^+ amplitudes increase.

The coherent production cross-sections for the different partial waves are obtained multiplying the total coherent cross-sections by the partial-wave fractions. The dependence on $\bar{A}$ of these cross-sections, integrated up to $t' = 0.01$ (GeV/c)^2 [$\overline{t'} = 0.01$ (GeV/c)^2 in formula (5)], has been fitted using the

Kölbig-Margolis-Glauber model (see Section 5). The best fit values of the parameter σ_2 are displayed in Table 7.

The values of σ_2 for the 1^+ state are systematically smaller than those of the total sample, and $\sigma_2(0^-)$ and $\sigma_2(2^-)$ are definitely larger.

7. CONCLUSIONS AND DISCUSSION

The more important results of the experimental analysis described in this paper can be summarized as follows:

i) The differential cross-sections are reproduced very well and in detail by the optical model, in the small-t' region, where the coherent contribution is dominant.

ii) The fits of the Kölbig-Margolis-Glauber formula on ($d\sigma/dt'$ versus t' versus A) and (σ_{coher} versus A) are good and very stable. The same best fit values, both of them fitting the differential cross-sections or the coherent cross-sections integrated in different t' ranges, are obtained for the parameter σ_2, which measures the absorption in nuclear matter.

iii) The partial-wave contributions show different behaviours for the different nuclear targets. The absorption in nuclear matter for 1^+ waves (1^+S, 1^+P, 1^+D) is definitely smaller than the best fit values obtained for 0^- (0^-S, 0^-P) and for 2^- amplitudes (2^-S, 2^-P). At 40 GeV incident energy it is depressed with respect to the absorption found for 1^+ at 15 GeV [2-4] and 22 GeV [5-8]. Because 1^+ is the dominant state, it follows that the absorption for the total sample is small.

iv) The contribution of the spin-flip is negligible [15].

It is impossible to disentangle a clear physical interpretation of these results; we can make only speculations.

On the one hand, the distribution of the production for the hadronic system taken as a whole is well represented within the framework of an optical model. On the other hand, the behaviour of the absorption in nuclear matter, as obtained using the Kölbig-Margolis-Glauber model, cannot be explained in a simple way.

We have observed that, for 0^- and 1^+ waves, not only the contributions, but also the relative phases change with t' and A [22].

One can think of an interference between at least two objects (either between two resonances or between a resonance and the background) with the same quantum numbers, or of an intermediate or transition state between the production collision and the completion of fixed states.

REFERENCES

[1] K.S. Kölbig and B. Margolis, Nucl. Phys. B6 (1968) 85, and references given therein.

[2] P. Mühlemann et al., ETH-Milan-CERN-Imperial College Collaboration, Nucl. Phys. B59 (1973) 106.

[3] G. Bellini, Proc. Topical Seminar on High-Energy Collisions Involving Nuclei, Trieste, 1974 (Editrice Compositori, Bologna, 1975), p. 317.

[4] W. Beusch et al., CERN-ETH-Imperial College-Milano Collaboration, Phys. Lett. 55B (1975) 97.

[5] T.J. Roberts et al., Phys. Rev. D 18 (1978) 59.

[6] R.M. Edelstein et al., Phys. Rev. Lett. 38 (1977) 185.

[7] W.C. Carithers et al., Proc. Topical Seminar on High-Energy Collisions Involving Nuclei, Trieste, 1974 (Editrice Compositori, Bologna, 1975), p. 307.

[8] W. Mollet et al., Phys. Rev. Lett. 39 (1977) 1646.

[9] L. Van Hove, Nucl. Phys. B46 (1972) 75.

[10] E.L. Feinberg, P.N. Lebedev Inst. of Physics, Reprint N 166 (1972).

[11] K. Gottfried, Acta Phys. Polon. B3 (1972) 769.

[12] W. Czyz and P. Zielinski, Coherent production on nuclei and measurements of total cross-section for unstable particles, Acta Phys. Polon. B11 (1980) 615.

[13] P. Osland and D. Treleani, Nucl. Phys. B107 (1976) 493.

[14] H.I. Miettinen and J. Pumplin, Phys. Rev. Lett. 42 (1979) 204; Phys. Rev. D 18 (1978) 1696.

[15] G. Fäldt and P. Osland, The role of two-step contributions in nuclear coherent and incoherent pion production, Arkiv for Det Fysik Seminar, Trondheim, No. 13 (1974).

[16] G. Fäldt, Proc. Topical Meeting on Multiparticle Production on Nuclei at Very High Energy, Trieste, 1976 (IAEA-SMR-21, Trieste, 1977), p. 387, and references given therein.

[17] P.L. Frabetti et al., Nucl. Instrum. Methods 148 (1978) 489.

[18] D. Menasce et al., PRAVDA: an interactive graphic system to scan and rescue events, Proc. Europhysics Conf. on Computing in High-Energy and Nuclear Physics, Bologna, 1980 (in preparation).

[19] Yu.M. Antipov et al., Nucl. Phys. B63 (1973) 141 and 153.

[20] G. Ascoli et al., Phys. Lett. 25 (1970) 962.

[21] J. Pernegr et al., Nucl. Phys. B134 (1978) 436.

[22] G. Bellini et al., Striking behaviour of the 0^- and 1^+ resonances of the coherently produced 3π system in the A_1 region, submitted to Physics Letters.

[23] C. Daum et al., Diffractive production of 3π states at 63 and 94 GeV, CERN-EP/80-219 (1980).

Table 1

Details of the model

$$\frac{d\sigma}{dt'} = \frac{d\sigma_c}{dt'} + \frac{d\sigma_I}{dt'} \quad \begin{cases} \dfrac{d\sigma_c}{dt'} = \dfrac{d\sigma_N}{dt'} A^2 |\tilde{F}(t',M)|^2 \\ \dfrac{d\sigma_I}{dt'} = I_0(M,A) S(t',M,A) \dfrac{d\sigma_N}{dt'} \end{cases}$$

$$\frac{d\sigma_N}{dt'} = C_0(M)\, e^{-B(M)t'} \quad or \quad \frac{d\sigma_N}{dt'} = C_0(M)$$

$$\tilde{F}(t',M) = 2\pi \int_{-\infty}^{+\infty} dz \int_{0}^{+\infty} db\, b \exp\left[i \frac{M^2 - m_\pi^2}{2p} z \right] J_0(\sqrt{t'} b) \rho(b,z) \exp\left[i\chi_{Coul}(b) \right]$$

$$\times \exp\left[-(1-i\alpha_1)\tfrac{1}{2}\sigma_1 T_1(b,z) \right] \exp\left[-(1-i\alpha_2)\tfrac{1}{2}\sigma_2 T_2(b,z) \right]$$

$$T_1(b,z) = \int_{-\infty}^{z} A\rho(b,z')\, dz' \; ; \quad T_2(b,z) = \int_{z}^{\infty} A\rho(b,z')\, dz'$$

$$\rho(r) = \rho_0 \left[1 + \exp \frac{r - c}{a} \right]^{-1} \; ; \quad \int \rho(\vec{r})\, d^3\vec{r} = 1$$

$$\chi_{coul}(b) = \frac{27}{137} \left\{ \ln (pb) + 4\pi \int_{b}^{\infty} \rho(r) \left[\ln \left(\frac{r}{b} + \sqrt{\frac{r^2}{b^2} - 1} \right) - \sqrt{1 - \frac{b^2}{r^2}} \right] r^2\, dr \right\}$$

Fixed parameters $\sigma_1 = 23.7$ mb $\qquad \alpha_1 = -0.15$

$B = 8.0\ (GeV/c)^{-2}$

$C = 1.12\ fm \times A^{1/3}$

$a = 0.545$ fm

α_2 is fixed, but a few different values are used: -0.5, 0, $+0.5$

Free parameters I_0, C_0, σ_2

Table 2

Fit on $d\sigma/dt'$ versus t' versus A with $d\sigma_N/dt' = C_0(M,p)\ e^{-B(M,p)t'}$

		$0.0 < t' < t^*$ (GeV/c)^2				$0.0 < t' < 0.5$ (GeV/c)^2			
		σ_2 (mb)	$\Delta\sigma_2$ stat.	C_0 (mb/GeV^2)	ΔC_0 stat.	σ_2 (mb)	$\Delta\sigma_2$ stat.	C_0 (mb/GeV^2)	ΔC_0 stat.
$1.0 < M_{3\pi} < 1.2$ GeV									
$\alpha_2 = 0$	B = 8.0 (GeV/c)$^{-2}$	16.9	±0.6	0.81	±0.02	16.9	±0.6	0.82	±0.02
$\alpha_2 = 0$	B free parameter BF = 8.16 ± 0.19					17.0	±0.6	0.82	±0.02
$\alpha_2 = -0.5$	B = 8.0					14.9	±0.5	0.79	±0.02
$\alpha_2 = +0.5$	B = 8.0					17.9	±0.6	0.84	±0.02
α_2 free parameter BF = -0.13 ± 0.09	B = 8.0					16.5	±0.6	0.82	±0.02
$1.2 < M_{3\pi} < 1.5$ GeV									
$\alpha_2 = 0$	B = 8.0 (GeV/c)$^{-2}$	15.4	±0.7	0.62	±0.02	15.2	±0.6	0.62	±0.02
$\alpha_2 = 0$	B free parameter BF = 7.97 ± 0.16					15.2	±0.6	0.62	±0.02
$\alpha_2 = -0.5$	B = 8.0					13.0	±0.5	0.60	±0.02
$\alpha_2 = +0.5$	B = 8.0					16.7	±0.7	0.63	±0.02
α_2 free parameter BF = 0.15 ± 0.11	B = 8.0					14.6	±0.8	0.61	±0.02
$1.5 < M_{3\pi} < 1.8$ GeV									
$\alpha_2 = 0$	B = 8.0 (GeV/c)$^{-2}$	17.2	±1.1	0.34	±0.01	17.0	±1.1	0.34	±0.01
$\alpha_2 = 0$	B free parameter BF = 8.38 ± 0.21					17.1	±1.1	0.34	±0.01
$\alpha_2 = -0.5$	B = 8.0					13.6	±0.8	0.31	±0.01
$\alpha_2 = +0.5$	B = 8.0					20.0	±1.3	0.35	±0.01
α_2 free parameter BF = 0.06 ± 0.15	B = 8.0					16.6	±1.5	0.35	±0.01

BF = best fit

Table 3

Fit on $d\sigma/dt'$ versus t' versus A with $d\sigma_N/dt' = C_0(M,p)$

	$0.0 < t' < t'^*$ (GeV/c)^2				$0.0 < t' < 0.5$ (GeV/c)^2			
	σ_2 (mb)	$\Delta\sigma_2$ stat.	C_0 (mb/GeV^2)	ΔC_0 stat.	σ_2 (mb)	$\Delta\sigma_2$ stat.	C_0 (mb/GeV^2)	ΔC_0 stat.
$1.0 < M_{3\pi} < 1.2$ GeV								
$\alpha_2 = 0$	16.2	±0.6	0.76	±0.02	16.1	±0.3	0.76	±0.02
$1.2 < M_{3\pi} < 1.5$ GeV								
$\alpha_2 = 0$	14.6	±0.6	0.58	±0.02	14.4	±0.6	0.57	±0.02
$1.5 < M_{3\pi} < 1.8$ GeV								
$\alpha_2 = 0$	16.5	±1.1	0.31	±0.01	16.1	±1.1	0.30	±0.01

Table 4

Fit on $\sigma_c(A,M)$ versus A with $d\sigma_N/dt' = C_0(M,p)\, e^{-B(M,p)t'}$

	$0.0 < t' < t'^*$ $(GeV/c)^2$					
	σ_2 (mb)	$\Delta\sigma_2$ stat.	$\Delta\sigma_2$ syst.	C_0 (mb/GeV^2)	ΔC_0 stat.	ΔC_0 syst.
$1.0 < M_{3\pi} < 1.2$ GeV						
$\alpha_2 = 0$	16.6	±0.7	+1.8 −0.9	0.81	±0.03	+0.08 −0.04
$\alpha_2 = -0.5$	14.3	±1.5		0.78	±0.06	
$\alpha_2 = +0.5$	17.8	±0.8		0.84	±0.03	
α_2 free parameter BF = 0.23 ± 0.43	17.4	±0.6		0.82	±0.03	
$1.2 < M_{3\pi} < 1.5$ GeV						
$\alpha_2 = 0$	15.4	±1.9	+1.5 −1.2	0.62	±0.05	+0.05 −0.04
$\alpha_2 = -0.5$	12.9	±1.5		0.60	±0.05	
$\alpha_2 = +0.5$	17.3	±2.0		0.64	±0.05	
$1.5 < M_{3\pi} < 1.8$ GeV						
$\alpha_2 = 0$	17.4	±1.9	+2.7 −0.8	0.35	±0.03	+0.05 −0.01
$\alpha_2 = -0.5$	13.7	±1.4		0.33	±0.02	
$\alpha_2 = +0.5$	20.8	±2.2		0.36	±0.03	

BF = best fit

Table 5

Fit on $\sigma_c(A,M)$ versus A with $d\sigma_N/dt' = C_0(M,p)$

	$0.0 < t' < t'^*$ (GeV/c)^2			
	σ_2 (mb)	$\Delta\sigma_2$ stat.	C_0 (mb/GeV^2)	ΔC_0 stat.
$1.0 < M_{3\pi} < 1.2$ GeV				
$\alpha_2 = 0$	15.2	±1.8	0.73	±0.06
$\alpha_2 = -0.5$	13.2	±1.5	0.71	±0.06
$\alpha_2 = +0.5$	16.4	±0.7	0.75	±0.03
α_2 free parameter BF = -0.2 ± 0.83	14.5	±3.5	0.73	±0.07
$1.2 < M_{3\pi} < 1.5$ GeV				
$\alpha_2 = 0$	14.1	±1.8	0.57	±0.05
$1.5 < M_{3\pi} < 1.8$ GeV				
$\alpha_2 = 0$	15.9	±1.8	0.31	±0.02

BF = best fit

Table 6

Partial wave contribution in % $[0.0 < t' < 0.01\ (GeV/c)^2]$

J^P	ℓ	Be + C	Al + Si	Ti + Cu	Ag + Ta + Pb
$0.9 < M_{3\pi} < 1.2$ GeV					
0^-	S	12.5 ± 1.2	12.5 ± 0.7	11.2 ± 1.6	9.6 ± 1.0
0^-	P	3.4 ± 0.8	2.3 ± 0.3	2.9 ± 0.7	2.0 ± 0.4
0^-	total	17.8 ± 1.7	16.4 ± 0.9	15.8 ± 2.1	12.8 ± 1.3
1^+	S	64.4 ± 3.4	64.8 ± 1.5	68.8 ± 3.6	66.9 ± 2.3
1^+	P	10.0 ± 1.2	10.4 ± 0.6	8.2 ± 1.2	9.8 ± 0.8
1^+	D	-	-	-	-
1^+	total	78.5 ± 2.3	80.9 ± 1.1	82.1 ± 2.8	85.3 ± 1.8
2^-	P	4.0 ± 1.5	3.0 ± 0.7	2.5 ± 1.3	2.1 ± 1.0
2^-	S	-	-	-	-
2^-	total	-	-	-	-
$1.2 < M_{3\pi} < 1.5$ GeV					
0^-	S	17.3 ± 2.2	14.4 ± 1.0	13.5 ± 2.2	9.4 ± 1.3
0^-	P	5.6 ± 1.0	5.4 ± 0.5	3.0 ± 0.9	3.8 ± 0.7
0^-	total	23.1 ± 2.7	21.0 ± 1.3	16.9 ± 2.6	13.7 ± 1.7
1^+	S	38.3 ± 3.1	37.5 ± 1.3	43.7 ± 3.1	50.9 ± 2.0
1^+	P	10.7 ± 1.7	13.1 ± 0.8	11.5 ± 1.6	10.6 ± 1.0
1^+	D	3.5 ± 0.8	3.1 ± 0.3	4.4 ± 1.0	4.3 ± 0.6
1^+	total	62.7 ± 3.2	66.8 ± 1.5	73.1 ± 3.3	79.7 ± 2.2
2^-	P	9.5 ± 1.8	7.9 ± 0.8	7.0 ± 1.7	3.4 ± 0.9
2^-	S	7.9 ± 1.3	4.3 ± 0.5	3.9 ± 1.2	2.3 ± 0.6
2^-	total	13.5 ± 1.9	11.3 ± 1.0	9.9 ± 2.1	5.0 ± 1.2
$1.5 < M_{3\pi} < 1.8$ GeV					
0^-	S	8.0 ± 3.1	10.5 ± 1.6	13.8 ± 4.5	13.3 ± 2.8
0^-	P	5.8 ± 2.9	2.1 ± 0.6	1.8 ± 1.3	2.3 ± 1.1
0^-	total	14.6 ± 4.0	13.2 ± 2.0	16.0 ± 5.2	15.9 ± 3.3
1^+	S	13.5 ± 2.8	15.0 ± 1.4	12.1 ± 3.2	14.9 ± 2.3
1^+	P	13.3 ± 2.6	17.2 ± 1.3	13.3 ± 2.9	14.0 ± 2.0
1^+	D	11.1 ± 2.3	12.6 ± 1.0	14.6 ± 2.8	16.2 ± 2.0
1^+	total	45.4 ± 4.6	52.2 ± 2.2	46.7 ± 5.5	53.1 ± 3.7
2^-	P	16.6 ± 3.1	12.2 ± 1.3	10.0 ± 2.8	10.0 ± 2.0
2^-	S	30.2 ± 3.0	28.0 ± 1.4	32.1 ± 3.5	26.1 ± 2.3
2^-	total	39.9 ± 3.9	34.5 ± 1.7	37.2 ± 4.2	31.1 ± 2.8

Table 7

$\sigma_2 \pm \Delta\sigma_2$ (mb) $[0.0 < t' < 0.01\ (GeV/c)^2]$

	$0.9 < M_{3\pi} < 1.2$ GeV	$1.2 < M_{3\pi} < 1.5$ GeV	$1.5 < M_{3\pi} < 1.8$ GeV
Total	16 ± 1	15 ± 1	18 ± 2
0^- S	21 ± 3	30 ± 6	9 ± 6
0^- P	28 ± 8	26 ± 9	63 ± 16
0^- total	23 ± 3	28 ± 5	16 ± 7
1^+ S	15 ± 1	9 ± 1	15 ± 5
1^+ P	15 ± 3	16 ± 4	17 ± 5
1^+ D	-	11 ± 2	11 ± 4
1^+ total	14 ± 1	11 ± 1	14 ± 2
2^- S	-	60 ± 19	21 ± 3
2^- P	33 ± 19	44 ± 12	31 ± 10
2^- total	33 ± 19	42 ± 10	23 ± 3

Figure captions

Fig. 1 : Experimental apparatus: a) the beam telescope; b) a general view of the set-up; c) details of the veto counter system, the counters, and the MWPC defining the trigger majority.

Fig. 2 : The differential cross-sections versus t' for the different nuclear targets and for the 3π mass interval 1.0-1.2 GeV. The crosses represent the experimental data; the vertical bars include the statistical errors and the uncertainty for inefficiency corrections, the horizontal ones correspond to a constant interval in the scattering angle. The full lines are the result of the fit of the Kölbig-Margolis formula on the differential cross-sections $d\sigma/dt'$ versus t' versus A.
The fit is done with the following conditions:
$\alpha_2 = 0.0$; $B = 8.0$ $(GeV/c)^{-2}$; $(d\sigma_N/dt')_{t'=0}$ is replaced in eq. (2) by the exponential (3); the Kölbig-Margolis equation is fitted in the full t' range 0.0-0.5 $(GeV/c)^2$. The σ_2 best fit value is 16.9 ± 0.6 mb. The broken lines represent the incoherent background calculated with the formula of Table 1 (see text).

Fig. 3 : The differential cross-section for the 3π mass interval 1.2-1.5 GeV. The fit conditions and the symbols are the same as in fig. 2. The σ_2 best fit value is 15.2 ± 0.6 mb.

Fig. 4 : The differential cross-sections for the 3π mass interval 1.5-1.8 GeV. The fit conditions and the symbols are the same as in fig. 2. The σ_2 best fit value is 17.0 ± 1.1 mb.

Fig. 5 : The differential cross-sections of the sample obtained with the tantalum target for the different mass intervals, plotted in the same figure for comparison.

Fig. 6 : The 3π invariant mass distributions for the samples with t' lower than the first diffractive minimum.

Fig. 7 : Total coherent cross-sections for different nuclear targets and for three mass intervals: 1.0-1.2, 1.2-1.5, and 1.5-1.8 GeV. The vertical bars include the statistical errors and the uncertainty for the inefficiency corrections. The full lines are the result of the fit on σ_c versus A with the Kölbig-Margolis equation integrated in t' up to the first diffractive minimum. The incoherent background has already been subtracted; α_2 and B are fixed [0.0 and 8.0 $(GeV/c)^{-2}$, respectively]. The best fit values for σ_2 are:
16.6 ± 0.7 for the 3π mass interval 1.0-1.2 GeV;
15.4 ± 1.9 for 1.2-1.5 GeV; and 17.4 ± 1.9 for 1.5-1.8 GeV.

Fig. 8 : Effective mass distributions of the main partial waves: 1^+S, 1^+P, 0^-S, 0^-P, 2^-S, and 2^-P, and of 1^+, 0^-, and 2^- total, for the coherent sample ($t' < t'^*$). The data are a compilation of events from all targets.

Fig. 9 : Dependence on t' of the more significant partial-wave contributions for the lightest and heaviest nuclear targets. Full lines: 1^+ total; dashed lines: 0^- total. The 3π mass intervals are 0.9-1.2 GeV in (a), and 1.2-1.5 GeV in (b).

Fig. 10 : Dependence on t' of the spin-flip percentages for the lightest and heaviest nuclear targets in three different 3π mass intervals: 0.9-1.2 GeV, 1.2-1.5 GeV, and 1.5-1.8 GeV.

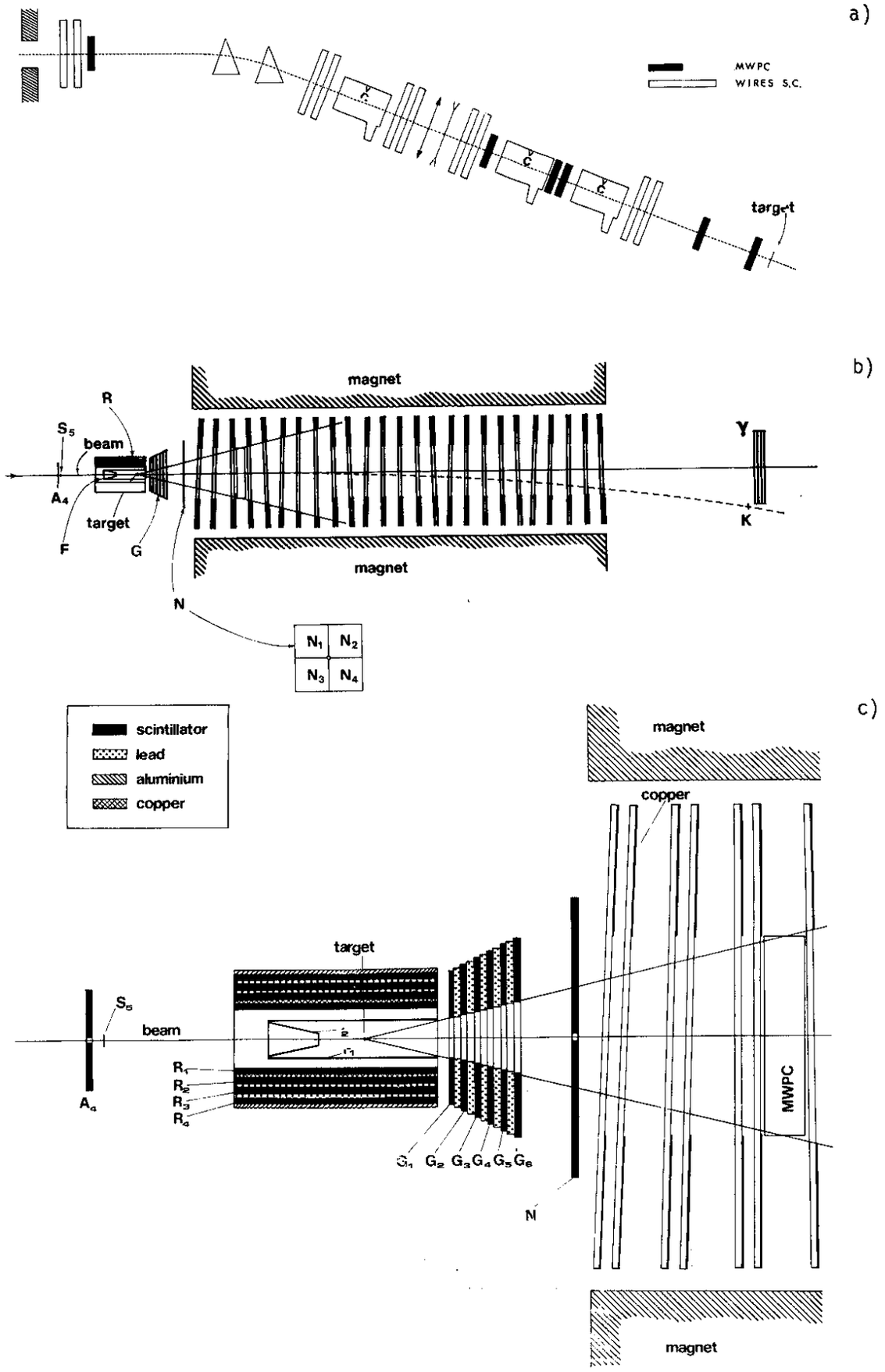
a)
MWPC
WIRES S.C.
target
b)
magnet
R
S5
beam
A4
target
F
G
magnet
Y
K
N
N1
N2
N3
N4
c)
scintillator
lead
aluminium
copper
magnet
copper
target
S5
beam
A4
R1
R2
R3
R4
G1
G2
G3
G4
G5
G6
N
MWPC
magnet

Fig. 1

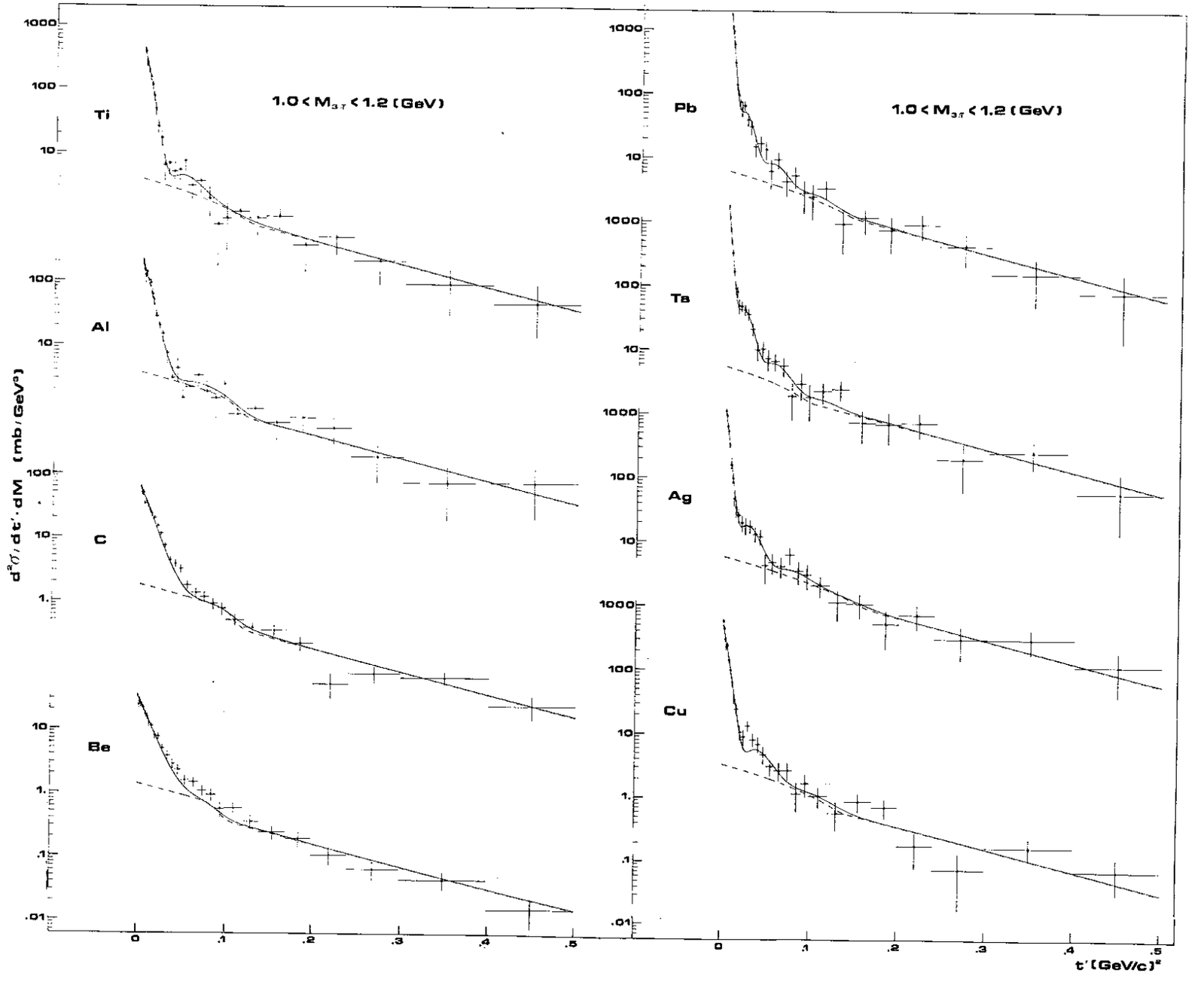

Fig. 2

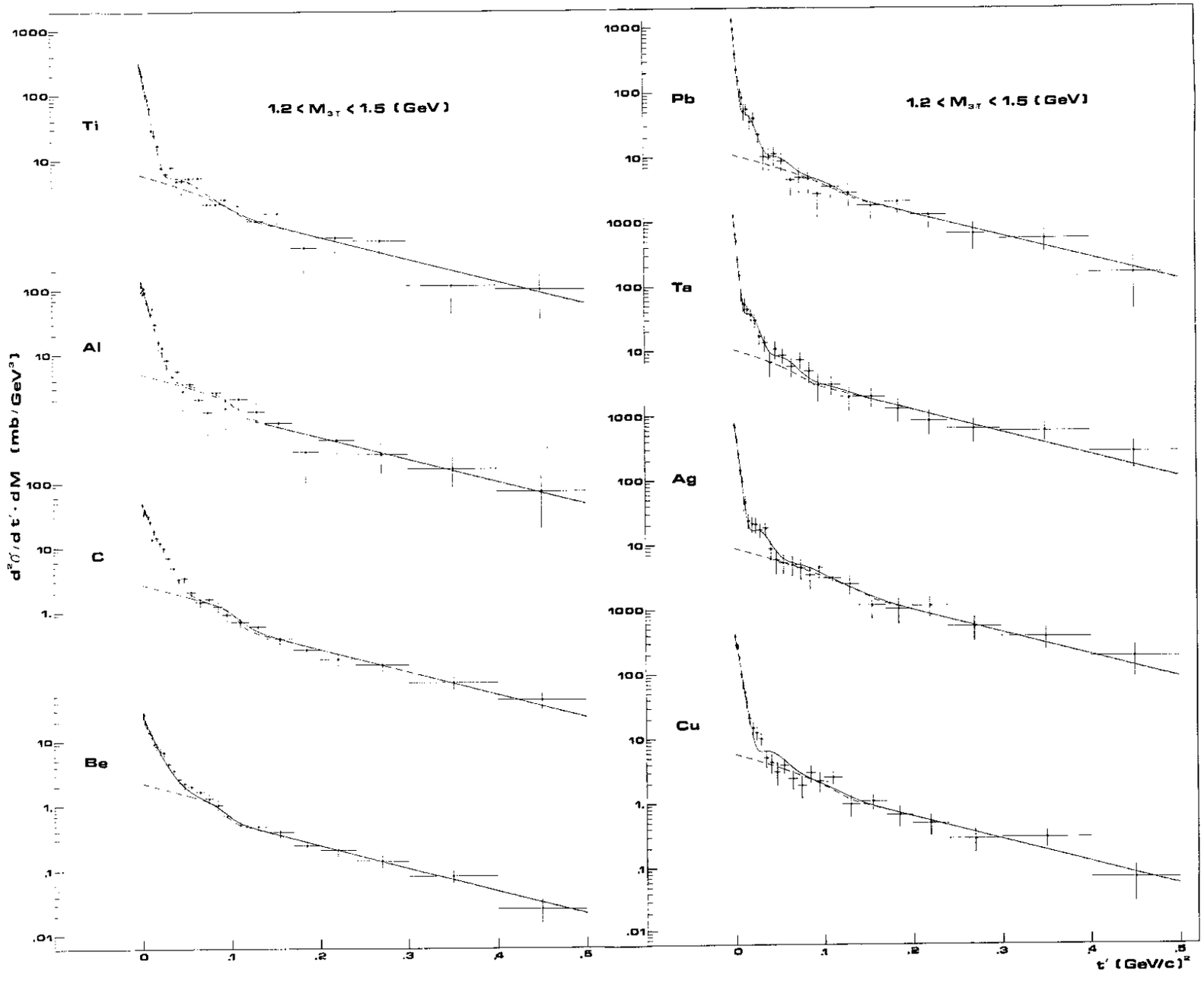

Fig. 3

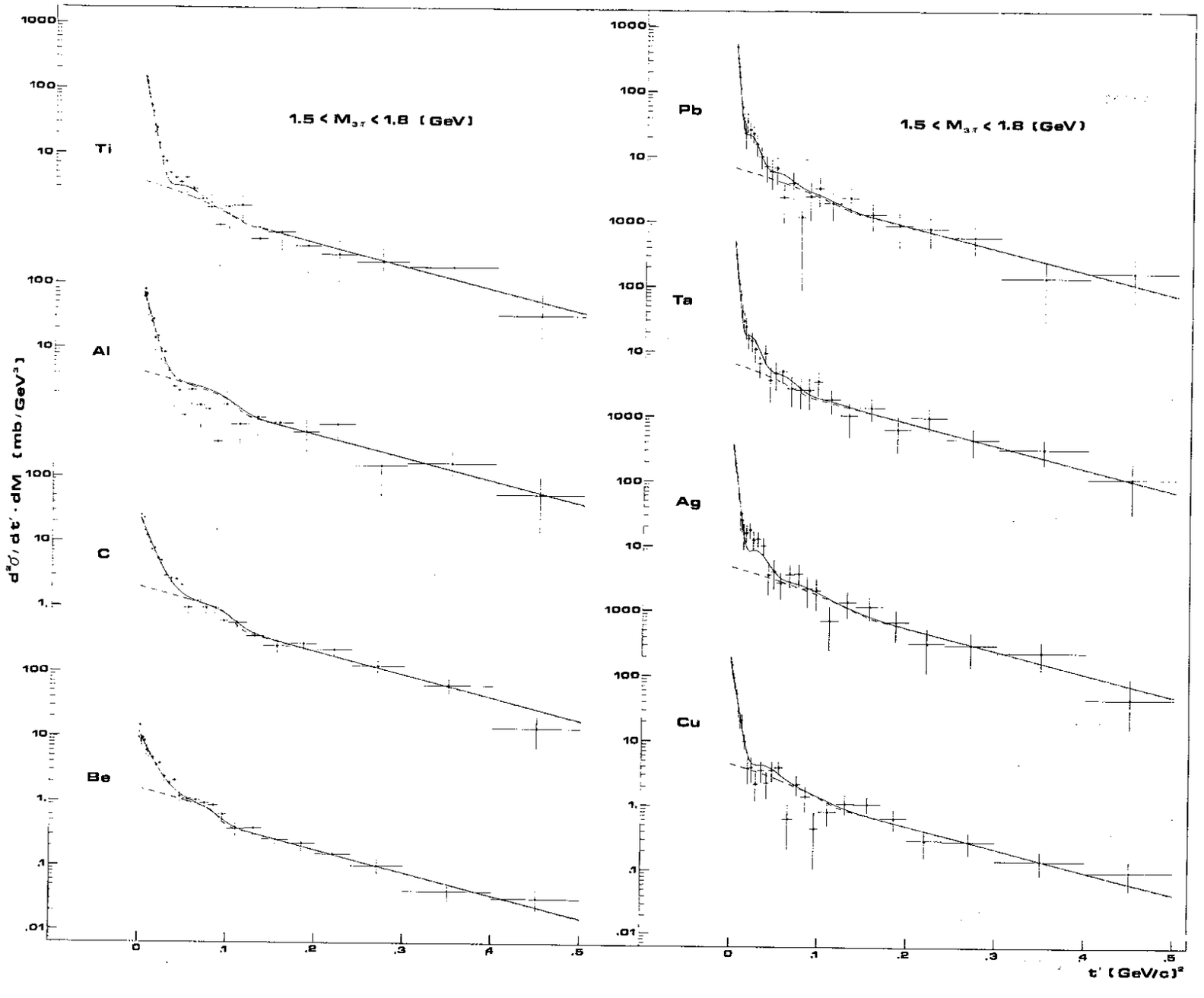

Fig. 4

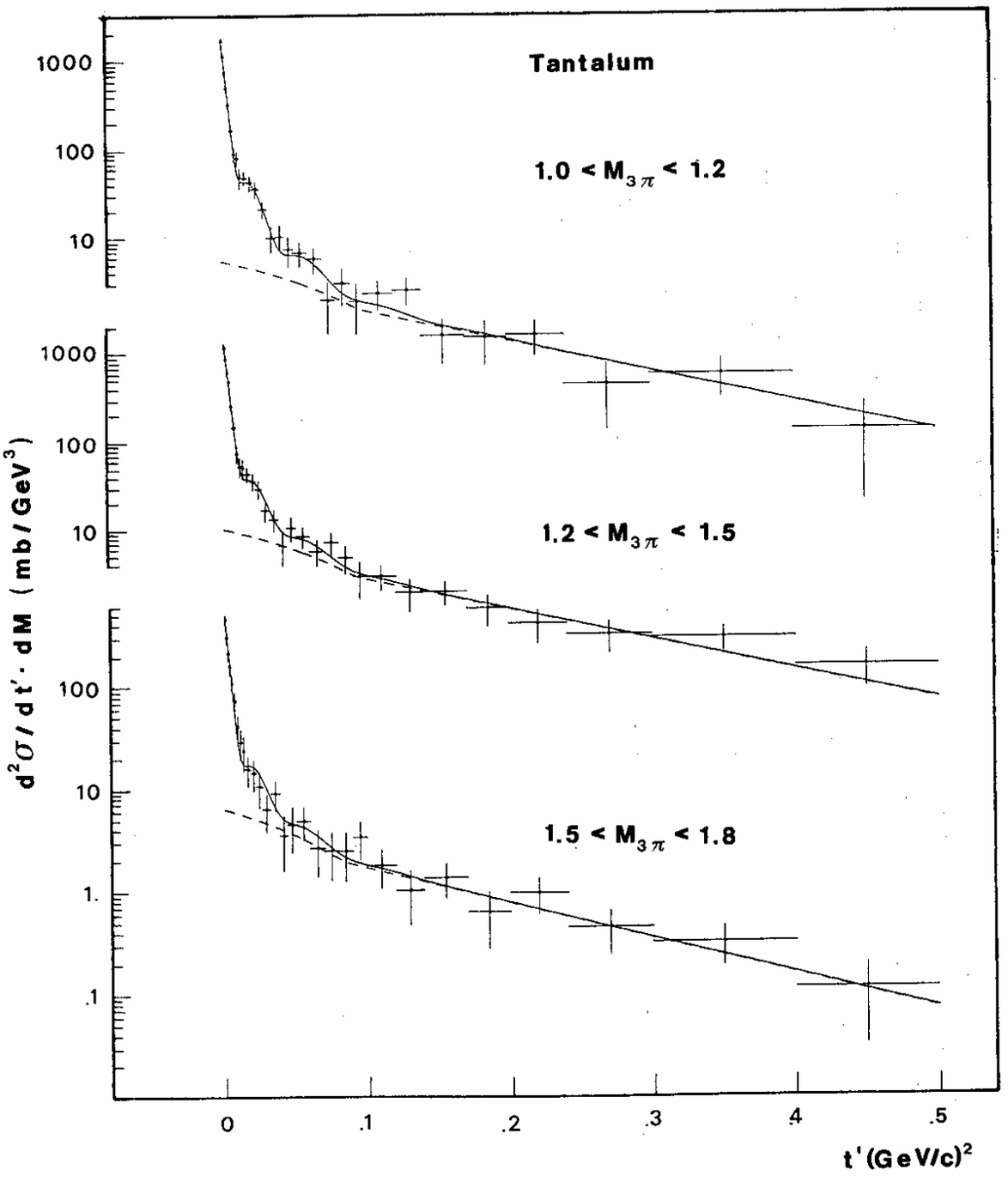
Tantalum
1.0 < M3π < 1.2
1.2 < M3π < 1.5
1.5 < M3π < 1.8
1000
100
10
1000
100
10
100
10
1.
.1
d²σ / dt' · dM (mb / GeV³)
0
.1
.2
.3
.4
.5
t' (GeV/c)²

Fig. 5

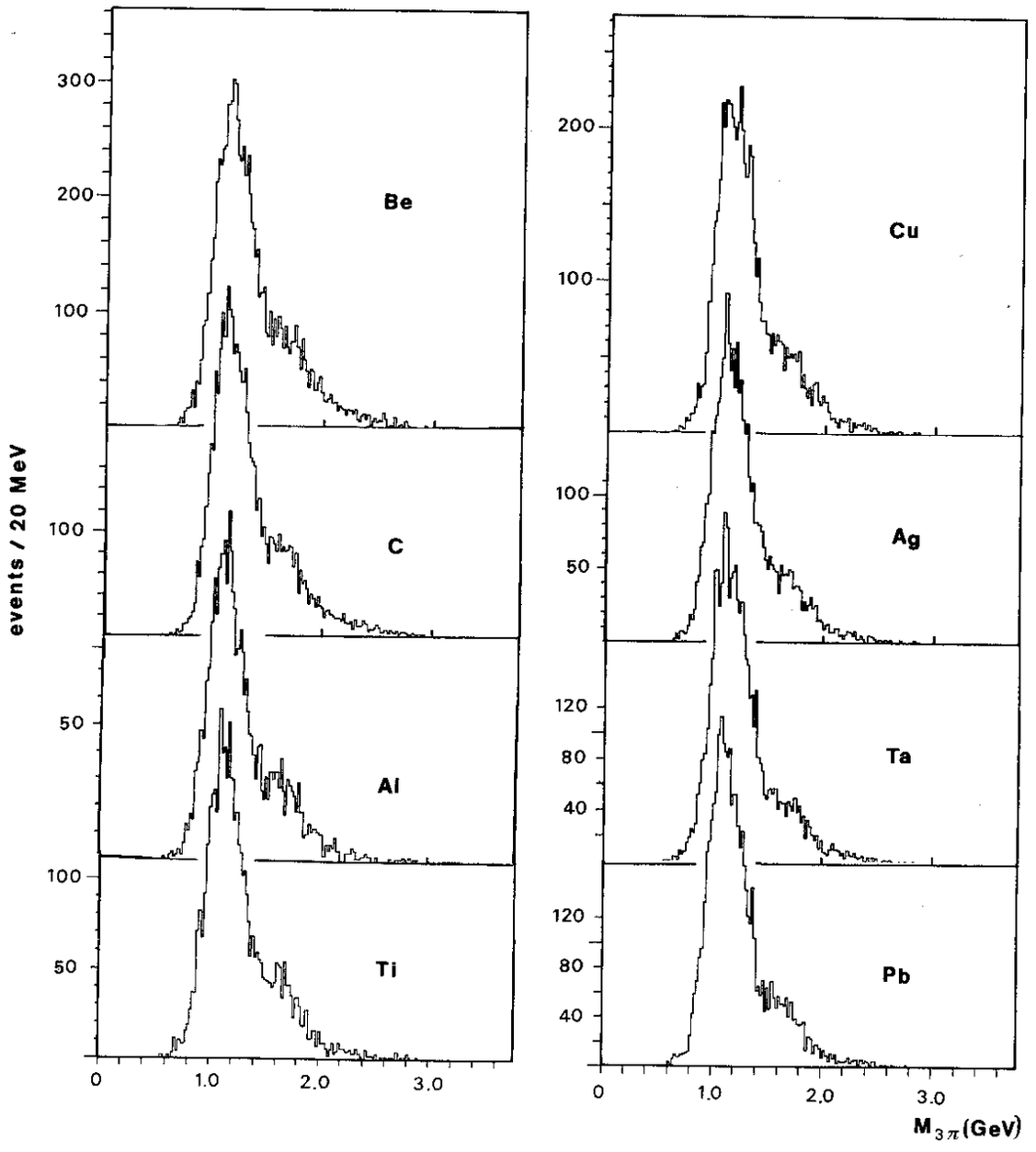

Fig. 6

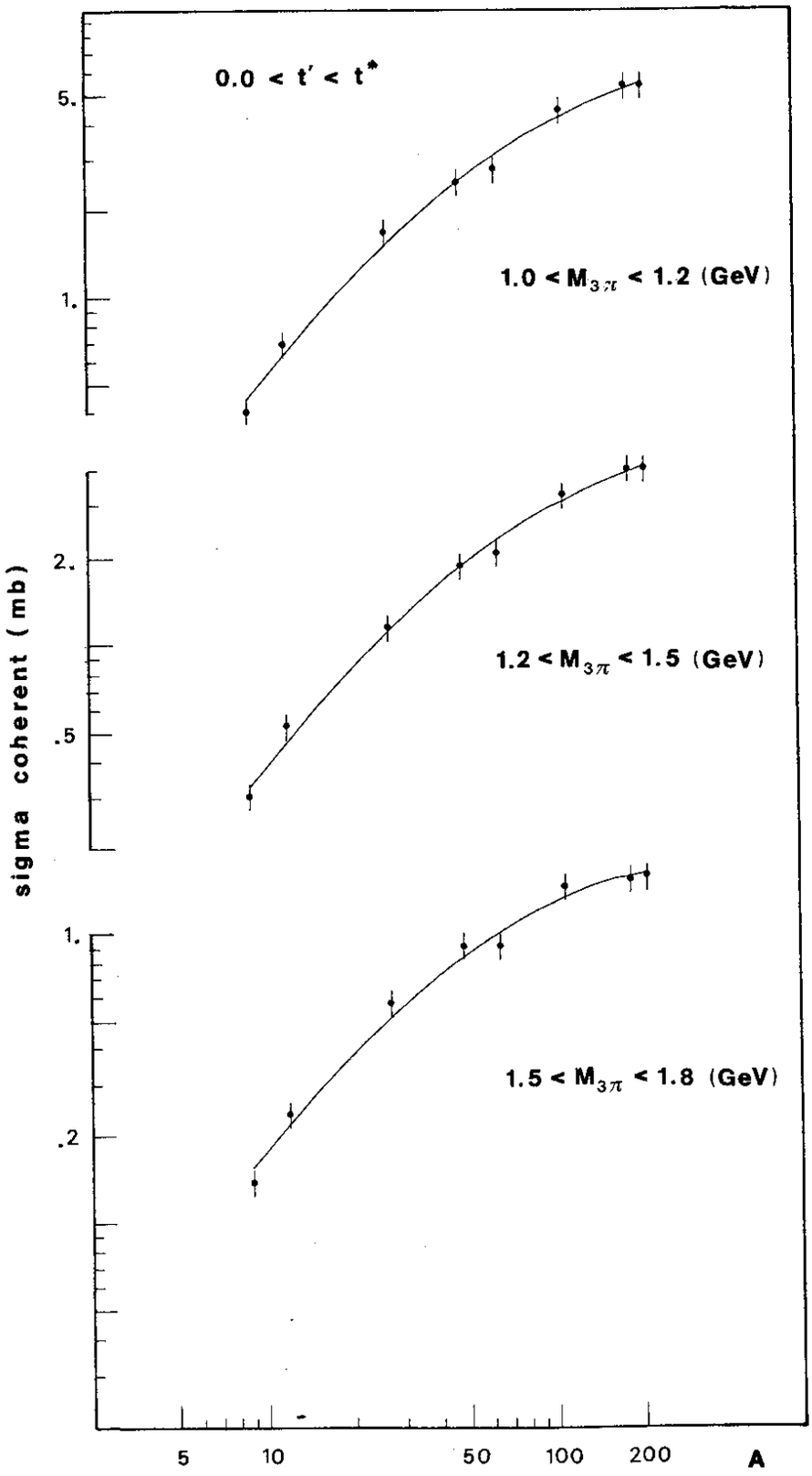
0.0 < t' < t*
1.0 < M3π < 1.2 (GeV)
1.2 < M3π < 1.5 (GeV)
1.5 < M3π < 1.8 (GeV)
sigma coherent (mb)
5.
1.
2.
.5
1.
.2
5
10
50
100
200
A

Fig. 7

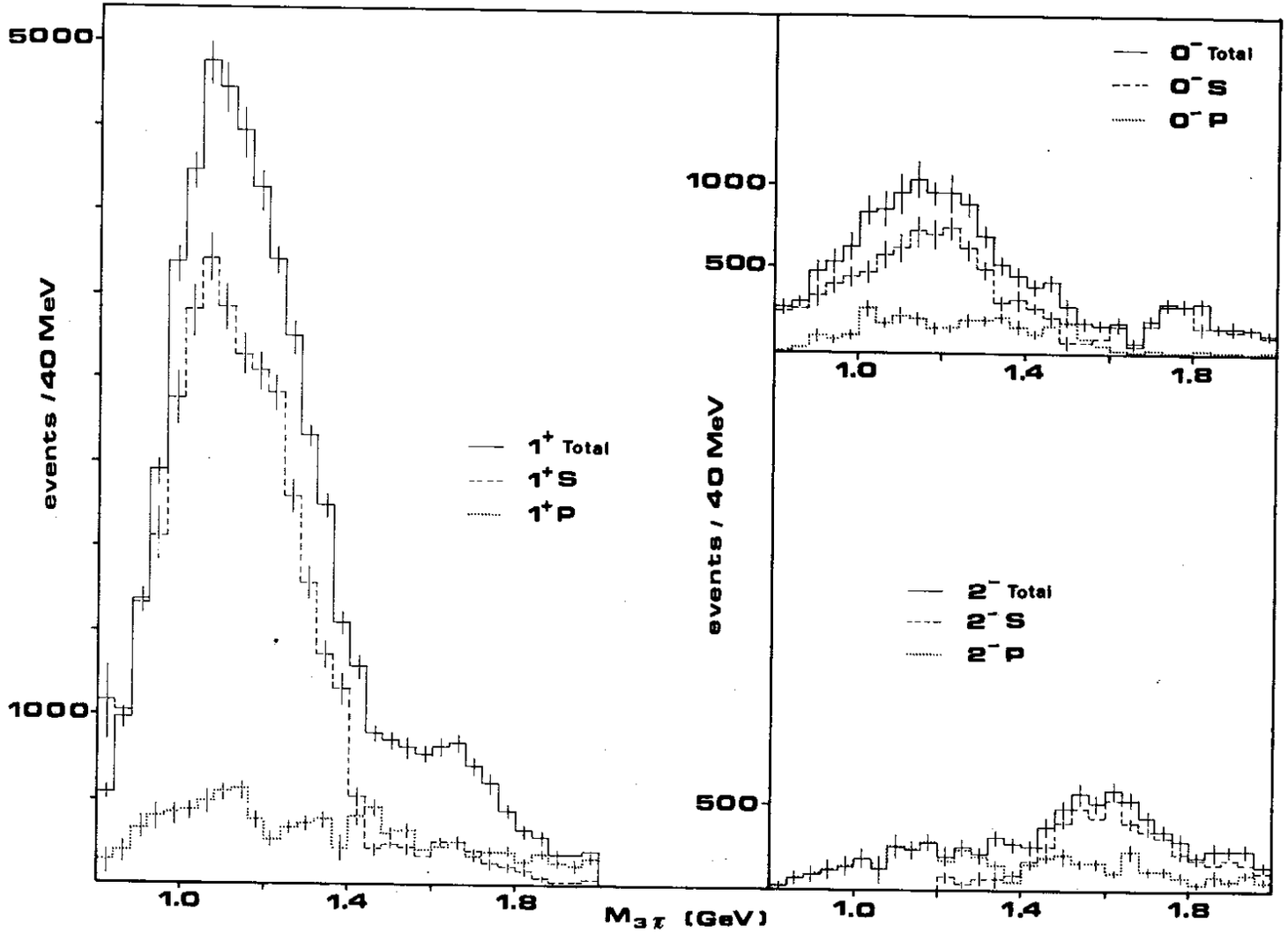
5000
1000
events / 40 MeV
1⁺ Total
1⁺S
1⁺P
1.0
1.4
1.8
M3π (GeV)
1000
500
events / 40 MeV
0⁻ Total
0⁻S
0⁻P
2⁻ Total
2⁻S
2⁻P

Fig. 8

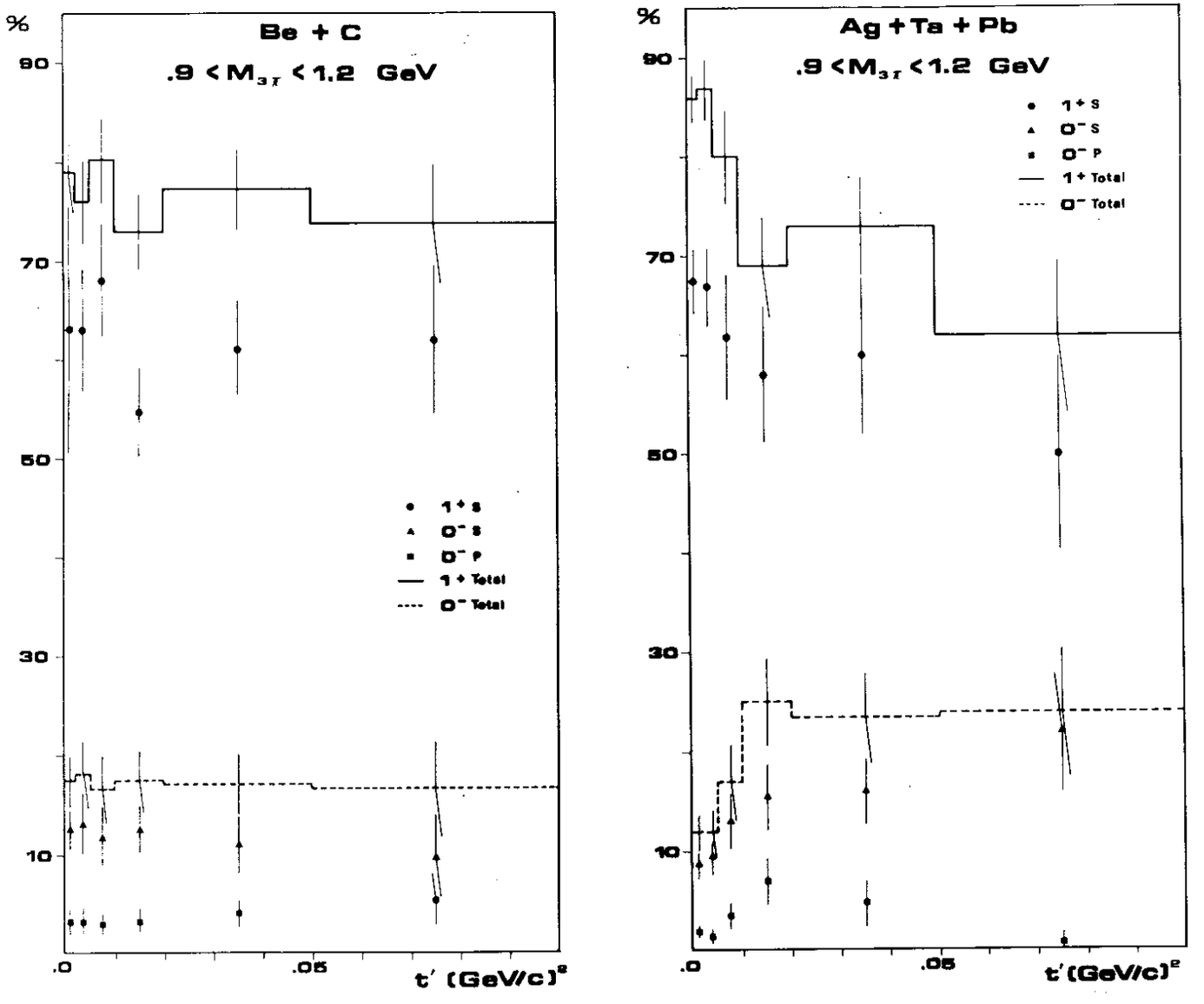
%
Be + C
.9 < M3π < 1.2 GeV
90
70
50
30
10
1+ S
0- S
0- P
1+ Total
0- Total
.0
.05
t' (GeV/c)²
%
Ag + Ta + Pb
.9 < M3π < 1.2 GeV
90
70
50
30
10
1+ S
0- S
0- P
1+ Total
0- Total
.0
.05
t' (GeV/c)²

Fig. 9a

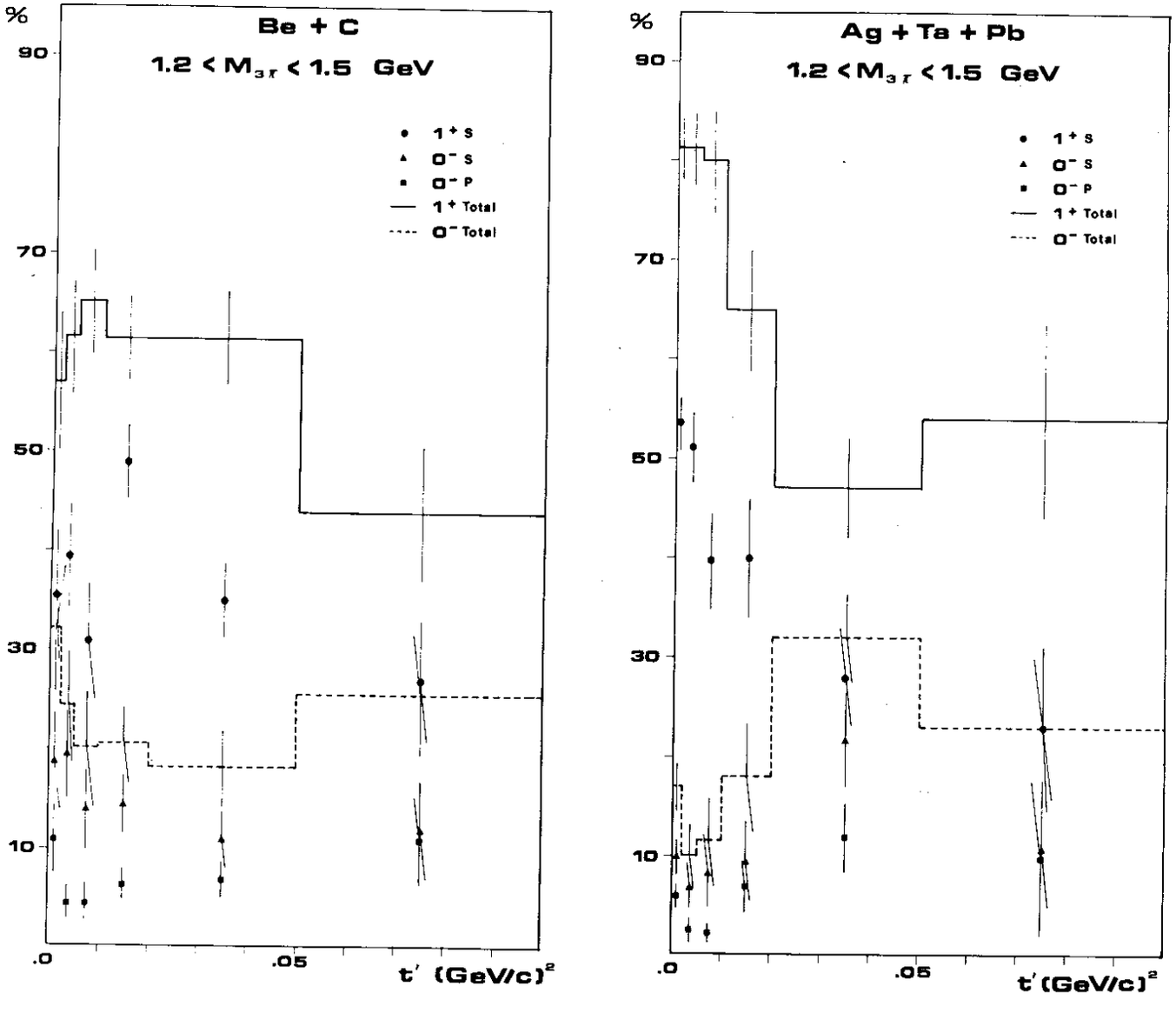
%
Be + C
1.2 < M3π < 1.5 GeV
1+ S
0− S
0− P
1+ Total
0− Total
90
70
50
30
10
.0
.05
t' (GeV/c)²
%
Ag + Ta + Pb
1.2 < M3π < 1.5 GeV
1+ S
0− S
0− P
1+ Total
0− Total
90
70
50
30
10
.0
.05
t' (GeV/c)²

Fig. 9b

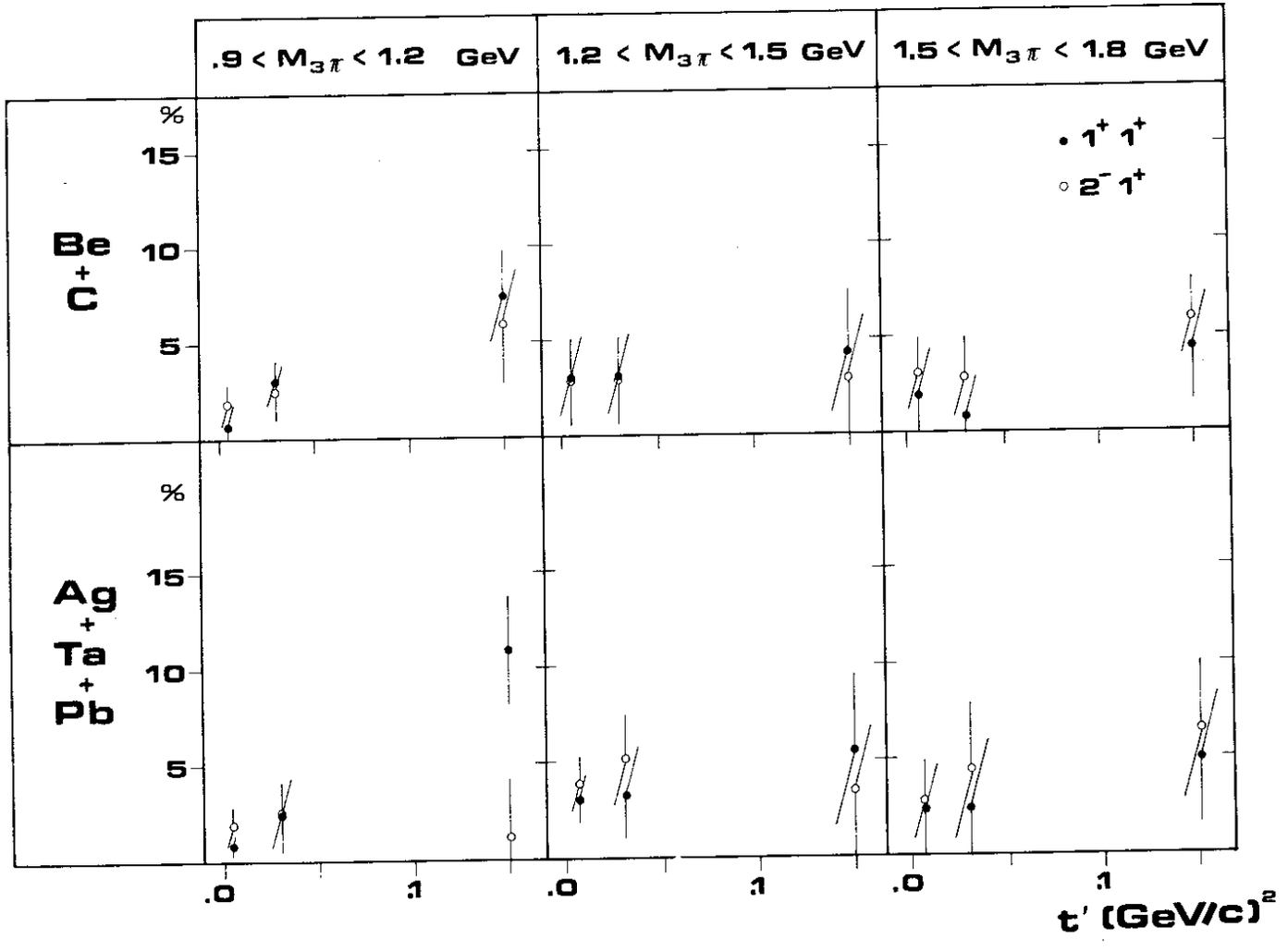
.9 < M3π < 1.2 GeV
1.2 < M3π < 1.5 GeV
1.5 < M3π < 1.8 GeV
• 1+ 1+
○ 2− 1+
Be + C
Ag + Ta + Pb
%
15
10
5
.0
.1
t' (GeV/c)²

Fig. 10